Flexible free-standing Ni-Mn oxides antennas decorated CNTs/nanofibers membrane for high-volumetric capacitance supercapacitors

Niranjala Fernando [†], Amutha Chinnappan [‡,], Atif. Aziz [§,*], Amor Abdelkader [†,*], Seeram Ramakrishna [‡], and Mark E. Welland [§]*

† Faculty of Science and Technology, Bournemouth University, Poole House, Talbot Campus, Poole, Dorset BH12 5BB

‡ Department of Mechanical Engineering, National University of Singapore, Singapore 117575, Singapore

§ Nanoscience Centre, Department of Engineering, University of Cambridge, CB3 0FF, UK.

* Corresponding authors

KEYWORDS: Ni-Mn oxides, carbon nanofibers, CNTs, flexible supercapacitor

ABSTRACT

There is a growing demand for lightweight flexible supercapacitors with high electrochemical performance for wearable and portable electronics. Here, we span nanoparticles of nickel - manganese oxide along with carbon nanotubes into carbon nanofibers and engineered a 3D

networked Ni-Mn oxides /CNT@CNF free-standing membrane for flexible supercapacitor applications. The electrospinning process controlled the nanoparticles aggregation while subsequent heat treatment generates the nanochannels in the fibres, resulting a very porous tubular nano composite structure. The preparation process also enabled good interfacial contact between the nanoparticles and the conductive carbon network. The resulted Ni-Mn oxides /CNT@CNF membrane displays a high mass loading (Ni-Mn oxides) of 855 mg cm^{-3} and a minimum CNTs incorporation as ~ 0.4 %. The outstanding porous structure, synergy of the carbon with Ni-Mn oxides, fast and facile faradic reactions on the electrode were responsible for the superior volumetric capacitance of 250 F cm^{-3} at 1 A cm^{-3}, energy density high as 22 mWh cm^{-3} and an excellent power density of 12 W cm^{-3}. Despite the low CNT loading, the hybrid electrode exhibits excellent cycling performance with a capacitance retention of 96.4 % after 10000 cycles evidencing a well-preserved Ni-manganese oxides nano structure throughout the cycling. The resulted outstanding electrochemical performances of Ni-Mn oxides /CNT@CNF synergic system offer new insights into effective utilization of transition metal oxides for establishing high-performance flexible super capacitors within a confined volume.

1. INTRODUCTION

The demand for miniaturised, portable and flexible energy storage devices has been enormously increasing due to their emergent applications in next-generation wearable electronics such as wrist mobile phones, curved screens and other portable electronic devices. [1, 2] Among the energy storage devices, supercapacitors and flexible supercapacitors (FSCs) had been taken significant attention owing to their outstanding electrochemical properties such as high power density (10 kW kg^{-1}), long cycle life (> 10^5 cycles), safe operation and low-cost fabrication etc.[3-7] Electrically

conductive, lightweight, thin and bendable material assemblies considered as ideal candidates for flexible SCs including a variety of carbonaceous materials for examples carbon nanofiber films [8, 9] graphene foams [10, 11] graphene papers [12-15] and carbon nanotube films [16, 17]. In the context of flexible SCs, areal/volumetric capacitance is more crucial than the gravimetric capacitance due to high demand for the thin electrodes. The current developments on FSCs mainly focus on boosting energy density and optimised performance in power density, cycle life and electrode flexibility and stability.

Among the carbonaceous electrodes for FSCs, carbon nanofibers (CNFs) obtained from electrospinning have been demonstrated as the most potential electrode for FSCs owing to their excellent electrical conductivity, high flexibility, and unique three-dimensional (3D) fibre web and capability to introduce electroactive nanomaterials into fibre network.[18, 19] On the other hand, electrospinning is a simple, effective and industrialised approach which widely used to synthesise freestanding CNFs membranes via a simple carbonisation process of polymer precursors. A self-standing web of CNFs can stand itself as a binder-free electrode saving considerable electrochemical performance loss from the binder.[20] However, sole utilisation of electrospun carbon nanofibers exhibited considerable limitations in capacitance and rate performances due to less active sites, limited surface area (4–40 m^2g^{-1}) and the shortage of the junction conductivity which established due to the poor connections between neighbouring fibres.[21] Therefore, the electrospinning technique has been directed towards in-situ incorporation of inorganic/ organic nanomaterials into the carbon fibres.[22, 23] For example, as an organic additive carbon nanotubes (CNTs) have been utilised widely due to their well-known massive applications in energy storage devices such as lithium-ion batteries, supercapacitors and flexible supercapacitors.[24, 25] Most importantly, CNTs incorporated CNFs make a remarkable composite by boosting electrochemical

conductivity and the enhanced active sites hence resulting the outstanding energy storage performances.[26, 27] However, the shortage of the capacitance and energy density limited the sole utilisation of CNF/CNT couple, and hence further research carried out with decorating the carbonaceous substrates with pseudocapacitive transition metal oxides such as manganese oxide [28-30] molybdenum oxide [31], titanium dioxide [32], nickel oxide [33, 34] and even ternary oxides like $NiMoO_4$ [35, 36], $NiCo_2O_4$ [37, 38], CuO [27] etc. In this combined approach of carbon together with metal oxides: high surface area and highly conductive 3 D fibre network of CNTs/ CNFs can efficiently hold the nanomaterials on the surface, and even metal oxides can be integrated into the carbonaceous matrix leading to increased electroactive sites, pseudocapacitance and even improved mechanical stability. [39-41] Most of the published composite where CNT was used to provide conductivity to the hybrid, the content of the CNT was usually above 1%. This added extra cost to the final composite and devices.

In the present study, we propose a simple electrospinning approach to synthesis Ni-Mn oxides nanoparticles/ CNTs@ CNFs composite as a synergistic system for a freestanding, flexible and high-performance electrode material for SCs. The idea of Ni incorporation is to alleviate the poor electrical intrinsic conductivity of Mn_3O_4 materials and hence enhance the capacitive performances. The binder-free Ni-Mn oxides / CNTs@ CNFs thin electrode films were prepared by electrospinning of polymer solution along with metal precursors and CNTs followed by oxidation, carbonisation and calcination. Also, the prepared composite has less CNT content than other similar electrodes in the literature, giving more space for the pseudocapacitance materials. In this approach, well dispersed and aggregated Ni-metal oxides are creating porous channels over the CNF surface while CNTs forms surface entangled antenna-like structures at the CNF web.

CNFs act as a binding network to both Ni-metal oxide nano particles and CNTs thus no need for binder and conductive carbon resulting in a flexible electrode.

As a result, Ni-Mn oxides /CNT@CNF nanocomposite exhibited outstanding flexible supercapacitor performances along with outstanding flexibility. The capacitive properties were demonstrated as the specific capacitance of 250 F cm^{-3} at 1 A cm^{-3}, an energy density of 22 mWh cm^{-3} and a power density of 12 W cm^{-3}, owing to the remarkable electrical conductivity, enhanced active sites and the synergic utilisation Ni and the pseudocapacitive phase of manganese oxide.

2. EXPERIMENTAL METHODS

2.1 Materials

All the materials used in this study were obtained from Sigma Aldrich. They include multi-walled carbon nanotubes (MWCNTs), polyacrylonitrile (PAN), N-N-dimethylformamide (DMF), Ni (II) acetate tetrahydrate 98% and Mn (II) acetate.

2.2 Fabrication of Ni-Mn oxides/CNT nanofibres

Solution preparation:

To prepare the electrospinning solution, initially, MWCNTs (0.05 w/w %) were dispersed in DMF (20 mL). The mixture was sonicated for 1 hr at 25 ºC to allow full dispersion of MWCNTs within the DMF solution. Then Mn (II) acetate and Ni (II) acetate tetrahydrate 98 % with weight percentage 2.0 % with respect to DMF) and PAN concentration of 10 % weight percentage (with respect to DMF) were added to the above solution simultaneously. Stirring was performed with a magnetic stirrer at 80 °C for 12 hr until a homogeneous electrospinable solution is formed.

Electrospinning:

To create electrospun fibres, MWCNTs/PAN/Mn/Ni solution was loaded into a plastic syringe of diameter 14.5 mm attached to a stainless-steel 18-gauge needle. The homogeneous solution contained in the plastic syringe was loaded perpendicularly to an earthed rotating drum covered with an aluminium foil sheet to allow the fibres to be collected. To electrospin, 22.0 KeV were applied between the needle and the drum collector. The distance between the collector and the need was 15 cm and the collector drum at the speed of 400 rpm. The polymer solution was feed at the rate of 1ml/h.

During electrospinning, jets of smooth PAN-based salt were observed to be ejected from the tip of the needle with minimal blockage of the opening. The ejection of the PAN-based salt together with the rotational motion of the drum over a period of 10 hr allowed the formation of several layers of nanowebs. The collected nanowebs were dried at 80 °C in the vacuum oven overnight in order to remove the solvent. Then it was stabilized at 300 °C with a heating rate of 2 °C /min for 2 hr in the air to pre-oxidise the MWCNTs/PAN/Mn/Ni salt into MWCNTs/PAN/ (Mn/Ni) O. This is to ensure that the nanofibres are maintained in their fibre form before being carbonized at high

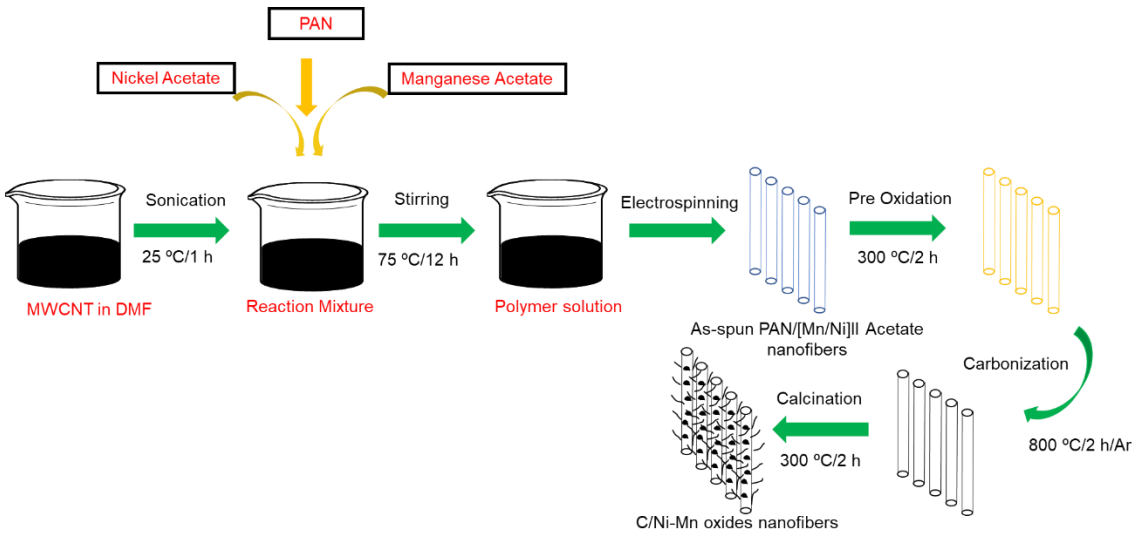

temperatures. The as-stabilized fibres were then carbonized under Ar gas for 2 hr at a heating rate of 5 °C /min at 800 °C. Lastly, the as-prepared nanofibres were further calcined at 300 °C under air for 2 hr at a heating rate of 2 °C/min to form Ni-Mn oxides /CNT@CNF nanofibres. The schematic representation is given in **Figure 1**.

Figure 1. A schematic diagram of the processing steps involved in creating Ni-Mn oxides /CNT@CNF electrospun nanofibres.

2.3 Material characterisation

The morphology and the nanostructure of nanocomposite thin films were evaluated using a scanning electron microscopy (FE-SEM, JEOL-6700F) fitted with an energy dispersive X-ray spectroscopy (SEM-EDS) at an accelerating potential of 15 KeV and transmission electron microscope (FE-TEM, JEOL JEM-2010F) at an accelerating potential of 200 KeV. The X-ray diffraction patterns were recorded in a 2θ range from 10° to 80° at 0.02° s^{-1} on a Bruker D8 advance diffractometer with Cu-Kα radiation of (λ=0.154 nm). The X-ray photoelectron spectroscopy (XPS, Kratos Axis ultra DLD spectrometer) was employed for the chemical structure evaluation. Thermogravimetric analysis (TGA) was performed on a Shimadzu DTG-60H under Ar with a heating rate of 10 °C min^{-1}. The N_2 sorption isotherms of the samples were measured at 77 K using ASAP 2020 to obtain the specific surface area and pore size distribution. Prior to adsorption/ desorption measurements, all samples were degassed at 200 °C for 12 h under vacuum. The specific surface area was calculated from the Brunauer– Emmett–Teller (BET) plot of the nitrogen adsorption isotherm and the pore size distribution of the samples was calculated from adsorption branch isotherms by Barrett–Joyner–Halenda (BJH) method.

2.4 Electrochemical measurements

The flexible self-standing Ni-Mn oxides/CNT@CNF composite membranes (1 cm×1 cm) were directly applied as symmetrical SC electrodes where 1 M KOH used as the electrolyte, pressed and ethanol cleaned two Ni foams were used as current collectors and a Whatman filter paper applied as the separator. The electrochemical performances were evaluated in a two electrode system using cyclic voltammetry (CV), galvanostatic charge-discharge (GCD) and electrochemical impedance spectroscopy (EIS) using an iviumstat electrochemical interface.

The specific volumetric capacitance (C_v) for the Ni-Mn oxides /CNT@CNF electrode was calculated form the $C_v = 4(I\Delta t/m\Delta V)$, where I is the constant discharge current, Δt is the time of discharging, m is the total material's weight in two electrodes and ΔV is the discharge voltage.[42] The energy density (E) and power density (P) for the supercapacitor cell was estimated from the $E = ½*C_v*\Delta V^2/3.6$ and $P = E*3600/\Delta t$ respectively.[43, 44]

3. RESULTS AND DISCUSSION

3.1 Structural characterisation

The flexible Ni-Mn oxides/CNT@CNF freestanding electrodes were developed by a three-step procedure as illustrated in **Figure 1** which includes, electrospinning of PAN, MWCNTs with $Ni(Ac)_2$ and $Mn(Ac)_2$ precursors, pre-oxidation at 300 °C , and carbonisation in an Ar environment at 800 ℃. The pre-oxidation process in the air makes composite fibres denser and more stabilised through the partial dehydrogenation reactions, which protects the porous structure during the subsequent carbonisation procedure. The polymer pyrolysis during the carbonisation evolves volatile substances as by-products, leaving porous hierarchical structures. The calculated specific surface areas of the Ni-Mn oxides/CNT@CNF composite film was 466 m^2 g^{-1} with an average pore diameter of ~ 1.7 nm and a total pore volume of 0.29 cm^3 g^{-1}. The excellent surface area

indicated that the incorporation of CNF/CNT matrix is beneficial to control the aggregation of Ni-Mn oxides nano particles achieving an effective ion diffusion into the inner region of the electrodes.

The XRD technique determined the crystal structure and phases of Ni-Mn oxides/CNT@CNF as in **Figure 2.** The prominent diffraction peak at 26. 43° can be indexed to the hexagonal graphite structure (JCPDS card 00-008-0415) with an interlayer d-spacing of 0.337 nm, indicating the carbonisation successfully produced crystalline carbon materials.[45, 46] The rest of the diffraction show the presence of Mn_3O_4 (hausmannite), Ni and formation of some $NiMn_2O_4$ (spinel) phase. The broaden behaviour of the XRD peaks could be arise from the smaller size of the nanostructures. The diffraction peaks at 32.5° and 36.19° shows the (103) and (211) planes of the tetragonal Mn_3O_4 with a d-spacing of 0.25 and 0.28 nm respectively (hausmannite, JCPDS card, 00-001-1127).[47, 48] Similarly for the Ni, the diffraction peak at 44.48 ° corresponds to the (111) crystal phase of cubic Ni with a d-spacing of 0.20 nm. The rest of the peaks at 51.83 ° and 76.35°can be referred to (200) and (220) planes of cubic Ni (JCPDS card, 01-070-1849). [49] In addition, $NiMn_2O_4$ spinel cubic phase was identified with major diffraction peaks at 30.56°, 35.98° and 43.65° corresponding to the (2 0 0), (3 1 1) and (4 0 0) planes with d-spacing values of 0. 29 nm, 0.25 nm and 0.21 nm respectively. (JCPDS card, 71-0852)[50-52]. The peaks experienced a very poor intensity indicating the low crystallinity of the $NiMn_2O_4$ along with a very low mass loading. The formation of $NiMn_2O_4$ can be explained through the doping of Ni^{2+} ions in to the Mn_3O_4 lattice and the similar oxidation states of the Mn^{2+} and Ni^{2+} and the comparable ionic radii of the ions (Mn^{2+} (0.80 Å), Ni^{2+} (0.69 Å)) further evidence this process. In addition, the presence of secondary phases well known to be enhancing the conductivity of metal oxides in supercapacitor

application and the binary oxides like $NiMn_2O_4$ may provide capacitive properties as an added benefit. [53]

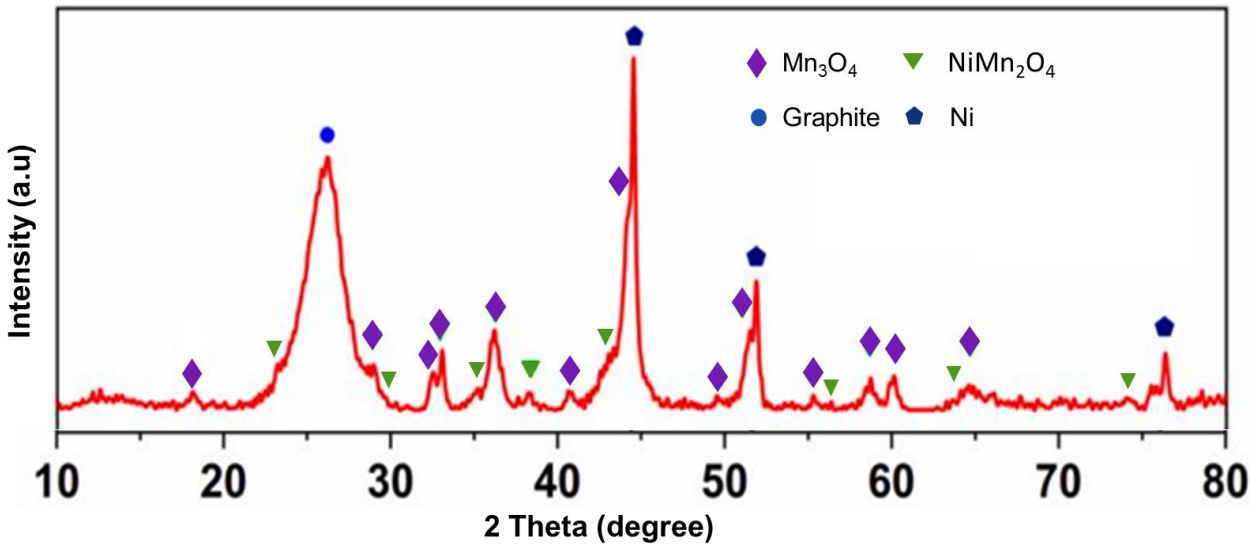

Figure 2. XRD pattern of Ni-Mn oxides /CNT@CNF nanocomposite.

The morphological and structural features of Ni-Mn oxides/CNT@CNF nanocomposite were examined using SEM technique. The as-spun fibre and the final porous composite fibre after calcination are presented in **Figure 3.** As illustrated in **Figure 3(a)** as spun nanocomposite fibres have smooth surfaces with diameters in the range of 500 to 700 nm. After calcination and carbonisation, the fibre surfaces seem to be becoming rough due to the polymer pyrolysis and the formation of crystalline Ni-Mn oxides nanocomposite. The average diameter of the fibres has been slightly reduced due to polymer decomposition during heat treatment and interestingly, the high magnification image of the CNF surface shows the growth of a large number of curly antennae-like Ni-Mn oxides over CNFs web **(Figure 3(b)).** The escape of the vapours and gases during the

pyrolysis process is particularly responsible for creating pores of several sizes, leading to the hierarchical porous tubular structures with the Ni-Mn oxides composite nanoparticles and CNTs are interconnected throughout the fibres (**Figure 3(c)**). These tubular nanoparticles would provide bonus active sites for the rapid access of KOH electrolyte ions in supercapacitors leading to an improved capacitance performance. Furthermore, SEM/EDX elemental mapping results of fibre composite (**Figure 3(d)**) confirms the presence of C, Mn, Ni and O elements and almost similar elemental distribution found for the Ni and Mn which alluding the occurrence of Ni-Mn oxides nanocomposite phase. Further confirmation of the elemental composition was obtained by SEM/EDX spectrum (**Figure S1**, supporting information). Finally, the electrospinning produced a mat of a 3D network of interconnected fibres, which kept its mechanical stability and integrity after the calcination and carbonisation, as shown from the low magnification image (**Figure S2**, supporting information).

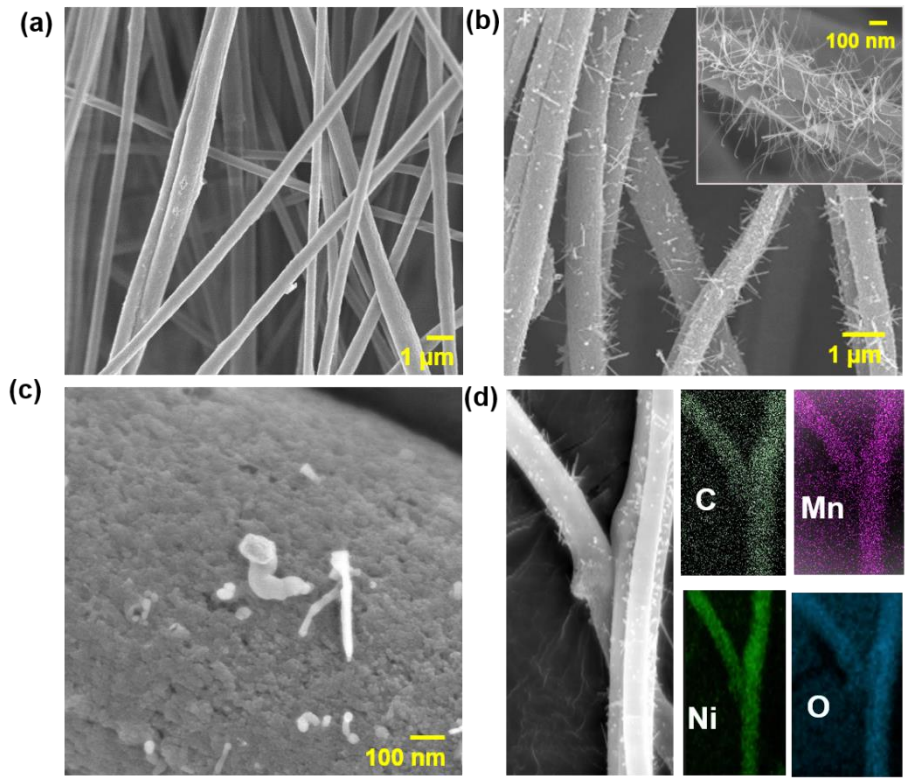

Figure 3. SEM micrographs of (**a)** as-spun fibres (**b)** calcined followed by carbonised fibres (inset shows the tangled Ni-Mn oxides antennas over the surface of CNF) (**c)** high magnification image of the CNF surface showing the porous nanoparticles coverage of Ni-Mn oxides and (**d)** EDX mapping of CNF composite.

TEM analysis can provide more details about the morphological and structural characterisation of the prepared composite fibres**.** Accordingly, **Figure 4 (a)** reveals a highly porous and fibrous structure of carbonised CNF with an approximate diameter of 500 nm. The surface of the CNF is rich in CNTs wrapping as can be observed in the magnified TEM image of **Figure 4 (b).** The high-resolution TEM image (**Figure 4(c)**) reveals the unbroken tangled CNTs with several mm length. The TEM micrographs in **Figure 4 (d)** illustrated a cubic nanoparticle of the Mn_3O_4 phase with an approximate diameter of 11 nm. **Figure S3** (supporting information) suggests that these oxides nanoparticles are interconnected to form the tubular structure. The lattice fringes of the predominant oxide phase inspected using HRTEM in **Figure 4 (e)** revealed a d-spacing value of 0.28 nm identified for the (103) plane of the tetragonal Mn_3O_4.[54] Furthermore, the selective area electron diffraction (SAED) pattern was taken for the Mn_3O_4 phase and results were compatible with the XRD pattern (**Figure 4 (f)**). In addition, some particles (**Figure 4(g)**) were identified with a d-spacing of 0.24 nm corresponding to the cubic crystal structure of the Ni (111) plane (**Figure 4(h)**. [55] Finally, the TEM images of the Mn_3O_4 antennas pointing out the fibres' surface (**Figure S4**, supporting information) indicate that the nanotubes are well connected to the fibre's carbon matrix, providing them with the required stability during the electrochemical charge/discharge cycles.

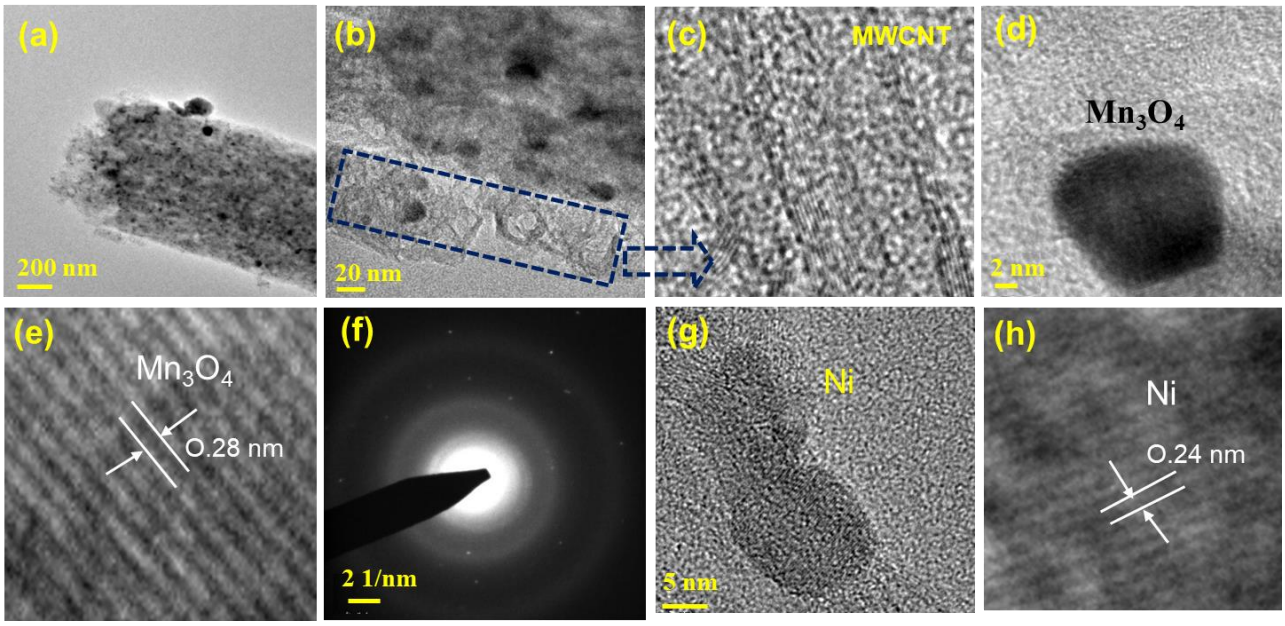

Figure 4. TEM micrographs of **(a)** fibre composite **(b)** an edge of a CNF surface showing the tangled CNTs antennas over the fibre surface **(c)** a HRTEM image of CNTs **(d)** a nanoparticle of Mn_3O_4 located on CNF surface **(e)** HRTEM image shows the d-spacing of 0.28 nm regarding the (103) plane of tetragonal Mn_3O_4 **(f)** SAED pattern of Mn_3O_4 **(g)** Ni nanoparticle located on CNF surface and **(h)** HRTEM image shows the d-spacing of 0.24 nm regarding (111) plane of cubic Ni phase.

The oxidation states and compositions of the as-prepared CNF composite was further evaluated by XPS spectra as illustrated in **Figure 5.** The survey XPS spectrum (**Figure 5(a)**) identifies the presence of C (1s), O (1s), Mn (2p) and Ni (2p) peaks, confirming the results of the SEM/EDX mapping. As presented in **Figure 5 (b)**, a typical CNTs/ CNFs C1s spectrum identified with a major binding energy peak at ~ 282 eV corresponding to sp^2 hybridised carbon, and low-intensity shoulder peaks at around 283 and 285 eV corresponding to sp^3 hybridised carbon and the C-O, C=O bonds, suggesting the oxides phases are chemically bonded to the carbon matrix.[56] The O 1s

spectrum showed binding energy peaks at 526 eV and 527 eV attributed to the oxygen in nickel oxide and manganese oxides. [57] The Ni 2p spectrum (**Figure 5(c)**) exists two binding energy states as at 871.5 eV and 854 eV corresponding to Ni 2p1/2 and Ni 2p3/2 configurations with two satellites which indicate the Ni^0 oxidation state while the presence of Ni-O binding peak could arise due to surface oxidation of Ni.[58-60] **Figure 5(d)**. illustrates the Mn 2p spectra with two major configurations of Mn 2p3/2 and Mn 2p1/2 equivalent to Mn^{2+} state at 636 eV, 649 eV and Mn^{3+} oxidation state at 640 eV and 652 eV confirming the Mn_3O_4 (**Figure 5(e)**). Furthermore, the Mn 3s XPS region (**Figure 5(f)**) shows the binding energy splitting width of 5.3 eV which is well-matched to the reported Mn_3O_4 spectra.[61-64] In addition, the Ni 2p3/2 peak located at 854 eV found to be combining with the Mn 2p3/2 and Mn 2p1/2 peaks and this phenomenon confirms the existence of Ni-Mn-O binary metal oxide phase.[65]

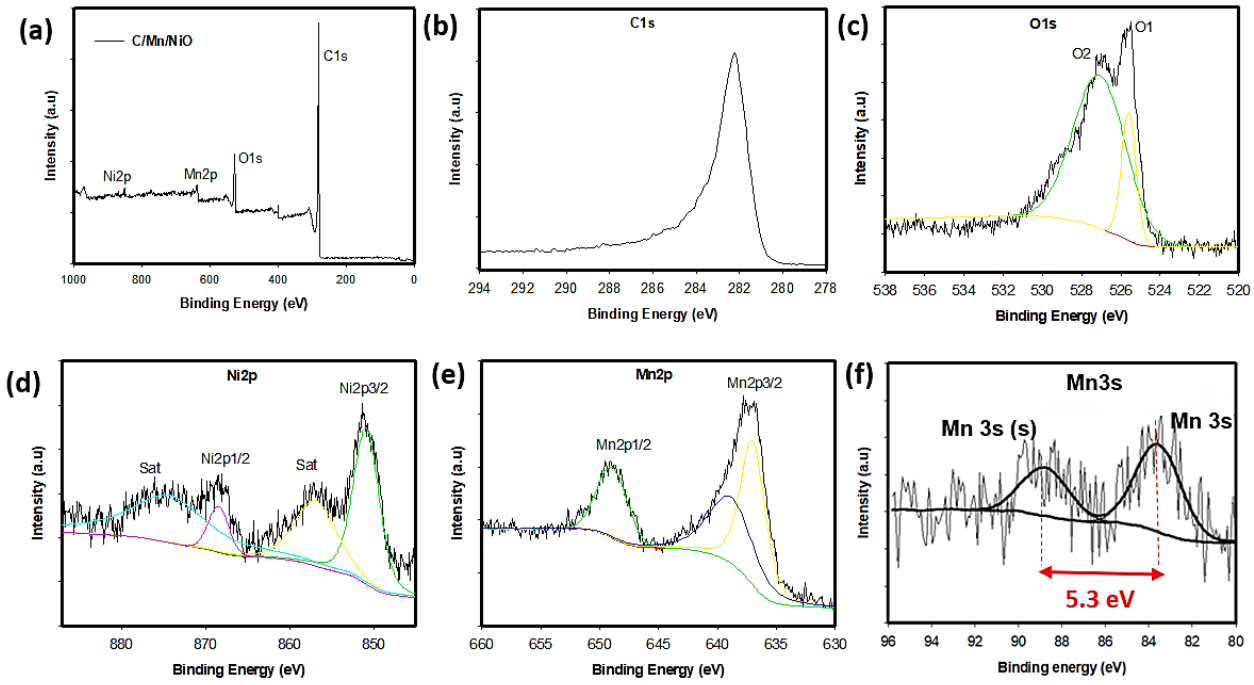

Figure 5. **(a)** XPS of Ni-Mn oxides/CNT@CNF **(b)** C 1s **(c)** O 1s **(d)** Ni 2p **(e)** Mn 2p and **(f)** Mn 3s regions.

Thermogravimetric analysis (TGA) was employed to obtain the carbon content, mass loading of Ni-Mn oxides and study the thermal stability of the hybrid system. Tests were run at a heating rate of 10 °C/min under Ar. As shown in **Figure 6**, as spun nanofiber/ CNTs composite experienced a complete decomposition of polymer materials at ~ 430 °C leaving residue of CNTs.[66] Accordingly, the Ni-Mn oxides/CNT@CNF composite (2.37 mg) showed a weight residue of ~ 1.66 mg at 800 °C demonstrating the composition of Ni-Mn oxides as 60 % with a mass loading of 855 mg cm^{-3}. Furthermore, the approximate CNTs composition in the composite was very low as ~ 0.4 %.

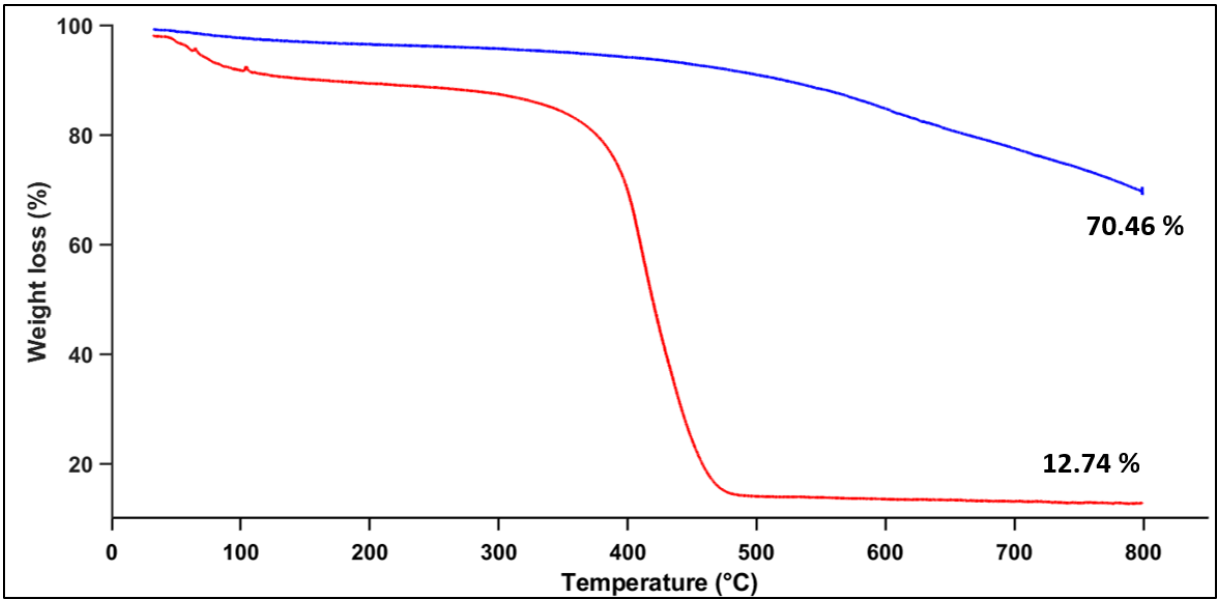

Figure 6. Thermogravimetric analysis of Ni-Mn oxides/CNT@CNF composite (blue) and the as-spun carbon nanofiber/ CNTs composite (red).

3.2 Electrochemical characterisation

The Ni-Mn oxides/CNT@CNF binder-free membrane showed an excellent flexibility as presented by **Figure 7(a)** photograph. Motivated by the outstanding mechanical stability and the flexibility, we assembled symmetrical supercapacitor devices by direct application of Ni-Mn oxides /CNT@CNF flexible self-standing membranes as electrodes, using pressed Ni foams as current collectors and applying a Whatman filter paper as a separator.

The CV analysis for the as build symmetrical SC was conducted in an electrolyte of 1 M KOH within a voltage window of **-** 0.4 – 0.4 V. The corresponding cyclic voltammograms at scan rates between 10 to 400 mV s^{-1} are presented in **Figure 7(b).** The Ni-Mn oxides/CNT@CNF electrode exhibited a clear and prominent electrochemical double-layer capacitive (EDLC) behaviour as indicated by the ideal rectangular/ symmetric CV curves. The prominent EDLC capacitive behaviour can be attributed to the electro-sorption of electrolyte ions on the CNFs/CNTs surfaces and the also a rapid pseudocapacitive contribution can be expected from the Ni-Mn oxides phase. In addition, the CV curves of the fibre composite appear to be maintaining their rectangular shape with increasing the scan rates, which evidence the facial electrosorption process on the electrode surface. The electrochemical behaviour of composites further characterised by galvanostatic charge-discharge (GCD) technique at a range of charge densities from 1 to 15 A cm^{-3} (**Figure 7(c)**. The characteristic symmetrical triangular curves were observed at a range of applied current densities indicating an excellent EDLC nature and a rapid faradic contribution of Ni-Mn oxides nanocomposite.[67] The specific volumetric capacitance (C_v) for the composite fibres, respect to the Mn_3O_4/CNT@CNF composite volume was evaluated from GCD curves at different current densities. The SC device was estimated an excellent volumetric capacitance of 250 F cm^{-3} at 1 A cm^{-3} and it was slightly decreased to 210 F cm^{-3} when the current density increased to 10 A cm^{-3}, suggesting a high rate capability (**Figure 7(d)**) [42] The incorporation of CNTs/ CNFs facilitate the

fast electrolyte ion diffusion in to the electrode interior while Ni/CNTs provide the excellent conductive pathways. These factors together confirm the resulted high rate capability of the Mn_3O_4/CNT@CNF synergic system. The energy density (E) and power density (P) of the flexible SC devices were also calculated and plotted in **Figure 7(e))**.[68] As can be seen, the Ni-Mn oxides/CNT@CNF composite exhibited an outstanding energy density of 22 mWh cm^{-3} and a maximum power of 12 W cm^{-3}. Similarly, the Mn_3O_4/CNT@CNF SC was delivered a maximum specific gravimetric capacitance of 187 F g^{-1} at a current density of 0.37 A g^{-1} and a high rate capacitance of 142 F g^{-1} at 7.5 A g^{-1}. Consequently, maximum energy of 16.6 Wh kg^{-1} and a power density 12 kW kg^{-1} were observed. (**Figure S5**, supporting information).

Moreover, the electrochemical impedance spectroscopy (EIS) analysis was applied to understand the capacitance resistance and charge transfer kinetics of the composite electrodes. The measurements were performed over the frequency range of 0.01 to 100 kHz.

Figure 7(f) illustrates the Nyquist plots of the EIS for the Ni-Mn oxides/CNT@CNF composite and an equivalent circuit model was applied to fit the impedance curve (inset of the **Figure 7 (f)**) where, R_s is the solution resistance, R_{ct} is the polarization resistance (charge transfer), C is the double layer capacitor and the Z is the Warburg impedance. [69] Accordingly a semicircle was observed at high-frequency range while a sloped line observed for the low-frequency range indicating an efficient ion diffusion between the electrolyte and the Ni-Mn oxides/CNT@CNF composite electrode surface.[70] The R_s was estimated to be ~ 0.35 Ω from the left intersection point of the semicircle. Similarly, the diameter of the semicircle signify the charge transfer resistance (R_{ct}) of electrode/ electrolyte interface which was calculated to be ~ 11.6 Ω for the Ni-Mn oxides/CNT@CNF composite electrode. The resulted R_{ct} value found to be comparable to recently reported Ni doped Mn_3O_4 supercapacitor.[71] In summary, the excellent volumetric capacitive

performance along with low electrode resistance and high charge transfer kinetics of Ni-Mn oxides/CNT@CNF composite electrode suggests great potential in wearable electronics.

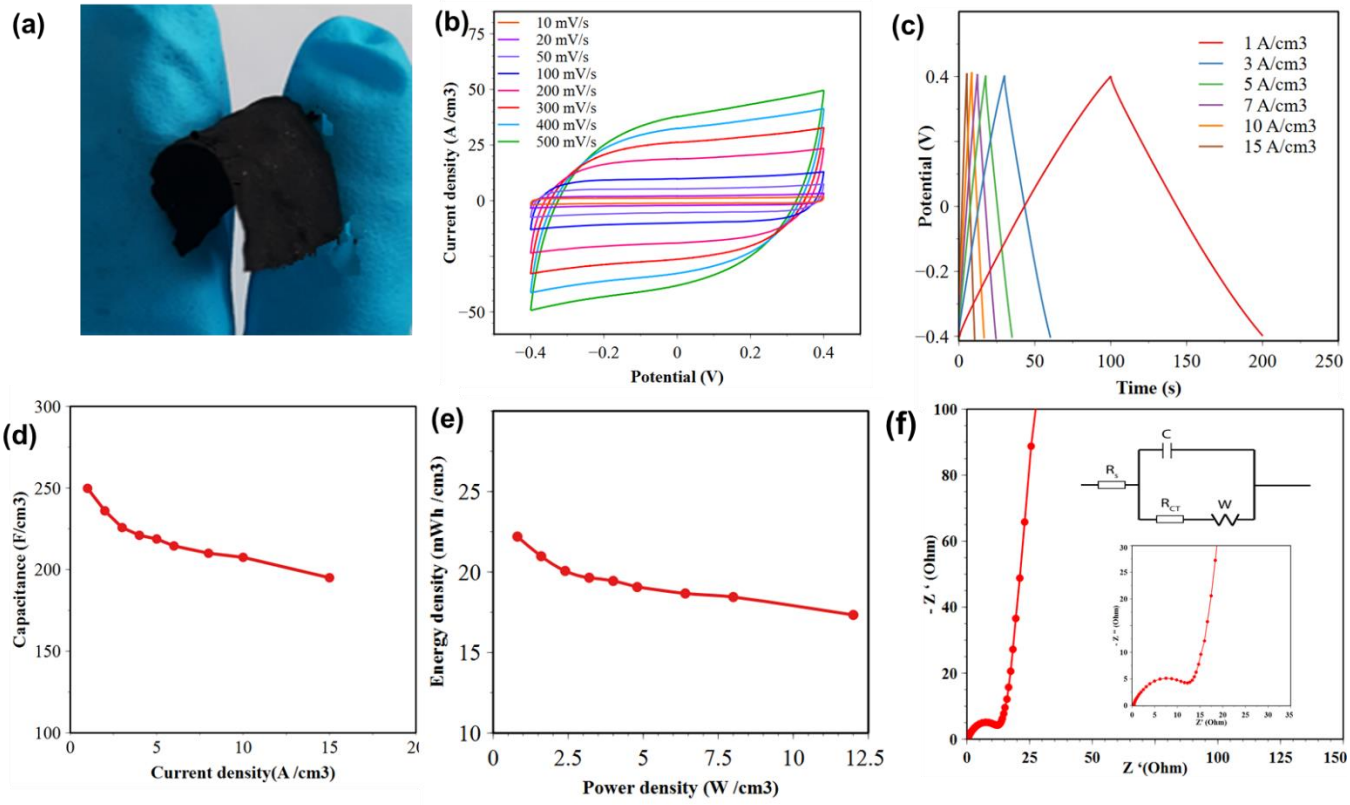

Figure 7. (a) Photographs of Ni-Mn oxides/CNT@CNF composite electrode showing its high flexibility **(b)** cyclic voltammograms at various scan rates of from 10 to 500 mV s^{-1} **c)** galvanostatic charge/discharge curves at different current densities from 1 to 15 A cm^{-3} **d)** specific areal capacitance at different current densities **e)** energy and power densities **f)** the electrochemical impedance spectroscopy (EIS) of the supercapacitor device (insets: corresponding equivalent circuit model and the magnified plot).

The supercapacitor device was cycled for 10000 cycles at a current density of 10 A cm^{-3} and retained about 96 % of its initial capacitance (**Figure 8)**. The carbonaceous network (CNTs, CNF) accountable for preserving the Ni- Mn oxides structure upon the long term cycling while Ni and CNTs could provide the promising electrical conductivity leading for an excellent capacitive performances.

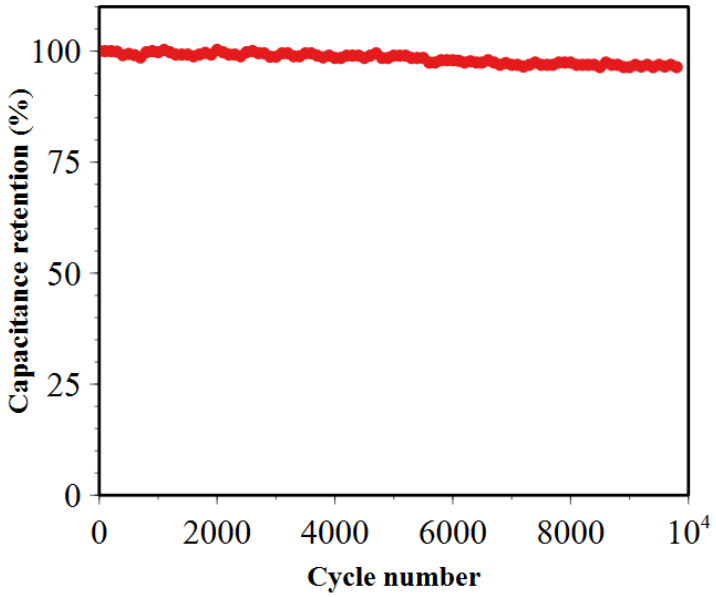

Figure 8. Cycling performance of Ni-Mn oxides/CNT@CNF supercapacitor device.

Table 1 compares the electrochemical performances of Ni-Mn oxides/CNT@CNF electrode with the reported Mn_3O_4 and Ni-Mn_3O_4 based supercapacitors. The symmetrical Ni-Mn oxides/CNT@CNF SC from our present work delivered a higher or comparable capacitance, energy density, power density and cycle stability to the previously reported Mn_3O_4 based supercapacitors. While it has been established that the electrochemical stability of the oxide-carbon composites is achieved at high carbon content, the developed electrode was able to maintain high cyclability with a very low CNT loading.

Table 1. Electrochemical performances of Mn_3O_4-based supercapacitor electrodes.

Material	Mass loading	Electrolyte	Capacitance	Capacitance retention/ Cycles	Energy and power densities	Ref.
Mn_3O_4/graphene	-	1 M Na_2SO_4	171 F g^{-1} at 0.1 A g^{-1}	93.2 % / 50	-	[72]
Mn_3O_4 /RGO paper	710 mg cm^{-3}	1 M Na_2SO_4	54.6 F cm^{-3} at 1 mV s^{-1}	85 % / 8000 at 2 A g^{-1}	5.5 mWh cm^{-3}, 10.95 W cm^{-3}	[73]
Asymmetric Mn_3O_4 /Ni graphite //$Ni(OH)_2$ /Ni graphite	1.0 mg cm^{-2}	PVA/ NaOH gel	3.05 F cm^{-3} at 5 mV s^{-1}	83 % / 12000 at 100 mV s^{-1}	0.35 mW h cm^{-3}, 32.5 mW cm^{-3}	[74]
Mn_3O_4 /rGO composite	1.1 mg cm^{-2}	1 M Na_2SO_4	351 F g^{-1} at 0.5 A g^{-1}	80.1 % /10000 at 5 A g^{-1}	-	[75]
Asymmetric Mn_3O_4/rGO//AC	1.1 mg cm^{-2}	1 M Na_2SO_4	66.18 F g^{-1} at 0.5 A g^{-1}	93 % / 5000 at 5 A g^{-1}	36.76 Wh kg^{-1}, 10 kW kg^{-1}	[75]
Porous Mn_3O_4 NPs	-	1 M Na_2SO_4	232.5 F g^{-1} at 0.5 A g^{-1}	78% / 5000 at 5 A g^{-1}	-	[76]
Mn_3O_4 NWs/CF	-	1 M Na_2SO_4	300.7 F g^{-1} and 571 mF cm^{-2} at 5 mV s^{-1}	100 %/7500 at 50 mV s^{-1}	41.7 Wh kg^{-1}, 79.4 mWh cm^{-2}	[77]
Ni-Mn oxides NPs /CNT@CNF	855 mg cm^{-3}	1 M KOH	250 F cm^{-3} at 1 A cm^{-3} and 187 F g^{-1} at 0.37 A g^{-1}	96.4 %/ 10000 at 10 A cm^{-3} or at 3.74 A g^{-1}	22 mWh cm^{-3} , 12 W cm^{-3} 16.6 Wh kg^{-1}, 12 kW kg^{-1}	This work

4. CONCLUSIONS

In summary, we have developed a flexible free-standing membrane of Ni-Mn oxides/CNT@CNF using interlinked nanofibres/CNTs with the nickel-manganese oxide spikes on the surface. The membrane was fabricated by a facile and easy to scale up electrospinning process followed by a calcination step. The electrospinning effectively hindered the agglomeration of the particles, and

the polymer pyrolysis during the calcination step created nanochannels, which together enlarged the contact area between the active material and the electrolyte, leading to a significant improvement in the kinetics of the faradic reaction. When used as a binder-free electrode in a symmetrical supercapacitor, the Ni-Mn oxides/CNT@CNF delivered a high volumetric capacitance of 250 F cm^{-3} at a current density of 1 A cm^{-3} with very low CNT content (0.4 %). In addition, the electrochemical stability was confirmed by the long cycle life of the device, which can be attributed to the ability of the porous electrode to accommodate the changes during the charge/discharge processes coupled with the high conductivity provided by the metallic Ni, graphitic carbon and CNTs in the composite.

ACKNOWLEDGMENT

The authors AC, SR. AA, and MEW acknowledge the support is given by Lloyd's Register Foundation, UK (grant no. R265000553597).

REFERENCES

1. N. Li, T. Lv, Y. Yao, H. Li, K. Liu and T. J. J. o. M. C. A. Chen, 2017, **5**, 3267-3273.
2. S. K. Ujjain, P. Ahuja, R. Bhatia and P. Attri, *Materials Research Bulletin*, 2016, **83**, 167-171.
3. H. Yu, J. Wu, L. Fan, Y. Lin, K. Xu, Z. Tang, C. Cheng, S. Tang, J. Lin and M. J. J. o. P. S. Huang, 2012, **198**, 402-407.
4. T. Liu, L. Zhang, W. You and J. J. S. Yu, 2018, **14**, 1702407.
5. T. Liu, L. Zhang, B. Cheng, W. You and J. J. C. C. Yu, 2018, **54**, 3731-3734.
6. A. M. J. J. o. M. C. A. Abdelkader, 2015, **3**, 8519-8525.
7. A. Abdelkader and D. J. N. Fray, 2017, **9**, 14548-14557.
8. L. Li, X. Zhang, Z. Zhang, M. Zhang, L. Cong, Y. Pan and S. J. J. o. M. C. A. Lin, 2016, **4**, 16635-16644.
9. Y. Li, H. Wang, L. Wang, Z. Mao, R. Wang, B. He, Y. Gong and X. J. S. Hu, 2019, **15**, 1804539.
10. H. Park, J. W. Kim, S. Y. Hong, G. Lee, D. S. Kim, J. h. Oh, S. W. Jin, Y. R. Jeong, S. Y. Oh and J. Y. J. A. F. M. Yun, 2018, **28**, 1707013.
11. Y. Zhao, J. Liu, Y. Hu, H. Cheng, C. Hu, C. Jiang, L. Jiang, A. Cao and L. J. A. m. Qu, 2013, **25**, 591-595.

12. H.-P. Cong, X.-C. Ren, P. Wang, S.-H. J. E. Yu and E. Science, 2013, **6**, 1185-1191.
13. G. Wang, X. Sun, F. Lu, H. Sun, M. Yu, W. Jiang, C. Liu and J. J. S. Lian, 2012, **8**, 452-459.
14. A. M. Abdelkader, N. Karim, C. Vallés, S. Afroj, K. S. Novoselov and S. G. J. D. M. Yeates, 2017, **4**, 035016.
15. S. Afroj, S. Tan, A. M. Abdelkader, K. S. Novoselov and N. J. A. F. M. Karim, 2020, **30**, 2000293.
16. S. Zeng, H. Chen, F. Cai, Y. Kang, M. Chen and Q. J. J. o. M. C. A. Li, 2015, **3**, 23864-23870.
17. J. Li, W. Lu, Y. Yan and T.-W. J. J. o. M. C. A. Chou, 2017, **5**, 11271-11277.
18. D. Lei, X.-D. Li, M.-K. Seo, M.-S. Khil, H.-Y. Kim and B.-S. J. P. Kim, 2017, **132**, 31-40.
19. Y. Huang, Y. Zhao, J. Bao, J. Lian, M. Cheng, H. J. J. o. A. Li and Compounds, 2019, **772**, 337-347.
20. L. Xu, P. Xiong, L. Zeng, Y. Fang, R. Liu, J. Liu, F. Luo, Q. Chen, M. Wei and Q. J. N. Qian, 2019, **11**, 16308-16316.
21. S. Yarova, D. Jones, F. Jaouen and S. J. S. Cavaliere, 2019, **2**, 159-176.
22. L. Zhang, Q. Ding, Y. Huang, H. Gu, Y.-E. Miao, T. J. A. a. m. Liu and interfaces, 2015, **7**, 22669-22677.
23. Q. Li, J. Guo, D. Xu, J. Guo, X. Ou, Y. Hu, H. Qi and F. J. S. Yan, 2018, **14**, 1704203.
24. Z. Chen, V. Augustyn, J. Wen, Y. Zhang, M. Shen, B. Dunn and Y. J. A. m. Lu, 2011, **23**, 791-795.
25. D. Zhou, X. Li, L.-Z. Fan and Y. J. E. A. Deng, 2017, **230**, 212-221.
26. H.-C. Hsu, C.-H. Wang, Y.-C. Chang, J.-H. Hu, B.-Y. Yao, C.-Y. J. J. o. P. Lin and C. o. Solids, 2015, **85**, 62-68.
27. F. Daneshvar, A. Aziz, A. M. Abdelkader, T. Zhang, H.-J. Sue and M. E. J. N. Welland, 2018, **30**, 015401.
28. T. Wang, D. Song, H. Zhao, J. Chen, C. Zhao, L. Chen, W. Chen, J. Zhou and E. J. J. o. P. S. Xie, 2015, **274**, 709-717.
29. Y. He, W. Chen, X. Li, Z. Zhang, J. Fu, C. Zhao and E. J. A. n. Xie, 2013, **7**, 174-182.
30. Y. Jin, H. Chen, M. Chen, N. Liu, Q. J. A. a. m. Li and interfaces, 2013, **5**, 3408-3416.
31. K. Tian, L. Wei, X. Zhang, Y. Jin and X. J. M. t. e. Guo, 2017, **6**, 27-35.
32. G. Tolba, M. Motlak, A. Bastaweesy, E. Ashour, W. Abdelmoez, M. El-Newehy and N. J. I. J. E. S. Barakat, 2015, **10**, 3117-3123.
33. Z. Gao, N. Song and X. J. J. o. M. C. A. Li, 2015, **3**, 14833-14844.
34. Y. Ouyang, X. Xia, H. Ye, L. Wang, X. Jiao, W. Lei, Q. J. A. a. m. Hao and interfaces, 2018, **10**, 3549-3561.
35. S.-W. Zhang, B.-S. Yin, C. Liu, Z.-B. Wang and D.-M. J. A. S. S. Gu, 2018, **458**, 478-488.
36. Y. Huang, F. Cui, Y. Zhao, J. Lian, J. Bao, H. J. J. o. A. Li and Compounds, 2018, **753**, 176-185.
37. G. M. Tomboc and H. J. E. A. Kim, 2019, **318**, 392-404.
38. J. Sun, W. Wang and D. J. J. o. E. M. Yu, 2019, **48**, 3833-3843.
39. Y. J. S. Dzenis, 2004, **304**, 1917-1919.
40. A. Greiner and J. H. J. A. C. I. E. Wendorff, 2007, **46**, 5670-5703.

41. Y. Huang, Y.-E. Miao, L. Zhang, W. W. Tjiu, J. Pan and T. J. N. Liu, 2014, **6**, 10673-10679.
42. M. D. Stoller, R. S. J. E. Ruoff and E. Science, 2010, **3**, 1294-1301.
43. J. Wang, X. Zhang, Q. Wei, H. Lv, Y. Tian, Z. Tong, X. Liu, J. Hao, H. Qu and J. J. N. E. Zhao, 2016, **19**, 222-233.
44. N. Hu, W. H. Gong, L. Huang and P. K. J. J. o. M. C. A. Shen, 2019, **7**, 1273-1280.
45. G. B. Loganathan, 2019.
46. M. H.-S. Ouaguenouni, A. Benadda, A. Kiennemann and A. Barama, *Comptes Rendus Chimie*, 2009, **12**, 740-747.
47. S. Majid, *Electrochimica Acta*, 2015, **175**, 193-201.
48. J. Hanawalt, H. Rinn, L. J. I. Frevel and E. C. A. Edition, 1938, **10**, 457-512.
49. J. Li, P. Li, J. Li, Z. Tian and F. Yu, *Catalysts*, 2019, **9**, 506.
50. M. Schubert, C. Münch, S. Schuurman, V. Poulain, J. Kita and R. J. S. Moos, 2018, **18**, 3982.
51. M. H.-S. Ouaguenouni, A. Benadda, A. Kiennemann and A. J. C. R. C. Barama, 2009, **12**, 740-747.
52. A. Ray, A. Roy, M. Ghosh, J. A. Ramos-Ramón, S. Saha, U. Pal, S. K. Bhattacharya and S. J. A. S. S. Das, 2019, **463**, 513-525.
53. A. Ray, A. Roy, M. Ghosh, J. Alberto Ramos-Ramón, S. Saha, U. Pal, S. K. Bhattacharya and S. Das, *Applied Surface Science*, 2019, **463**, 513-525.
54. X. Peng, Z. Wang, Z. Wang, Y. J. F. o. C. S. Pan and Engineering, 2019, **12**, 790-797.
55. P. Ahuja, S. K. Ujjain, R. K. Sharma and G. Singh, *RSC Advances*, 2014, **4**, 57192-57199.
56. R. A. Moraes, C. F. Matos, E. G. Castro, W. H. Schreiner, M. M. Oliveira and A. J. J. J. o. t. B. C. S. Zarbin, 2011, **22**, 2191-2201.
57. Y. H. Ahmad, K. A. Eid, S. Y. AlQaradawi, N. K. J. S. E. Allam and Fuels, 2017, **1**, 1123-1129.
58. Z. Zhang, A. Matsubayashi, B. Grisafe, J. U. Lee and J. R. Lloyd, *Materials Chemistry and Physics*, 2016, **170**, 175-179.
59. P. Prieto, V. Nistor, K. Nouneh, M. Oyama, M. Abd-Lefdil and R. Díaz, *Applied Surface Science*, 2012, **258**, 8807-8813.
60. D. Ji, J. Sun, L. Tian, A. Chinnappan, T. Zhang, W. A. D. M. Jayathilaka, R. Gosh, C. Baskar, Q. Zhang and S. Ramakrishna, *Advanced Functional Materials*, 2020, **30**, 1910568.
61. Y. Xu, X. Wang, C. An, Y. Wang, L. Jiao and H. Yuan, *Journal of Materials Chemistry A*, 2014, **2**, 16480-16488.
62. M. Harilal, S. G. Krishnan, A. Yar, I. I. Misnon, M. V. Reddy, M. M. Yusoff, J. Ojur Dennis and R. Jose, *The Journal of Physical Chemistry C*, 2017, **121**, 21171-21183.
63. M. C. Biesinger, B. P. Payne, A. P. Grosvenor, L. W. Lau, A. R. Gerson and R. S. C. Smart, *Applied Surface Science*, 2011, **257**, 2717-2730.
64. K. Dhanalaxmi, R. Singuru, S. K. Kundu, B. M. Reddy, A. Bhaumik and J. Mondal, *RSC advances*, 2016, **6**, 36728-36735.
65. M. C. Biesinger, B. P. Payne, A. P. Grosvenor, L. W. Lau, A. R. Gerson and R. S. C. J. A. S. S. Smart, 2011, **257**, 2717-2730.
66. N. D. Tissera, R. N. Wijesena, C. S. Sandaruwan, R. M. de Silva, A. de Alwis, K. N. J. M. C. de Silva and Physics, 2018, **204**, 195-206.

67. W. Li, J. Shao, Q. Liu, X. Liu, X. Zhou and J. Hu, *Electrochimica Acta*, 2015, **157**, 108-114.
68. C. Xiang, M. Li, M. Zhi, A. Manivannan and N. J. J. o. P. S. Wu, 2013, **226**, 65-70.
69. M. Zhang, Q. Li, D. Fang, I. A. Ayhan, Y. Zhou, L. Dong, C. Xiong and Q. J. R. a. Wang, 2015, **5**, 96205-96212.
70. G.-r. Xu, J.-j. Shi, W.-h. Dong, Y. Wen, X.-p. Min and A.-p. Tang, *Journal of Alloys and Compounds*, 2015, **630**, 266-271.
71. A. Naiknaware, J. Chavan, S. Kaldate and A. A. Yadav, *Journal of Alloys and Compounds*, 2019, **774**, 787-794.
72. Y. Fan, X. Zhang, Y. Liu, Q. Cai and J. J. M. L. Zhang, 2013, **95**, 153-156.
73. Y. Hu, C. Guan, G. Feng, Q. Ke, X. Huang and J. J. A. F. M. Wang, 2015, **25**, 7291-7299.
74. J.-X. Feng, S.-H. Ye, X.-F. Lu, Y.-X. Tong, G.-R. J. A. a. m. Li and interfaces, 2015, **7**, 11444-11451.
75. Z. Huang, S. Li, Z. Li, J. Li, G. Zhang, L. Cao, H. J. J. o. A. Liu and Compounds, 2020, **830**, 154637.
76. F. Yang, M. Zhao, Q. Sun and Y. J. R. A. Qiao, 2015, **5**, 9843-9847.
77. K. Sambath Kumar, J. Cherusseri and J. J. A. o. Thomas, 2019, **4**, 4472-4480.